PAPER

Check for updates

Close-packed silane nanodot arrays by capillary nanostamping coupled with heterocyclic silane ring opening†

Michael Philippi,[a] Changjiang You,*[bc] Christian P. Richter,[b] Mercedes Schmidt,[a] Jannis Thien,[d] Domenik Liße,[b] Joachim Wollschläger,[d] Jacob Piehler [ID] [b] and Martin Steinhart [ID] *[a]

We report the parallel generation of close-packed ordered silane nanodot arrays with nanodot diameters of few 100 nm and nearest-neighbor distances in the one-micron range. Capillary nanostamping of heterocyclic silanes coupled with ring-opening triggered by hydroxyl groups at the substrate surfaces yields nanodots consisting of silane monolayers with exposed terminal functional groups. Using spongy mesoporous silica stamps with methyl-terminated mesopore walls inert towards the heterocyclic silanes, we could manually perform multiple successive stamping cycles under ambient conditions without interruptions for ink refilling. Further functionalizations include the synthesis of polymer nanobrushes on the silane nanodots by surface-initiated atom-transfer radical polymerization. Proteins-of-interest fused to the HaloTag were site-specifically captured to silane nanodots functionalized by copper-free reactions with azide derivatives. Thus, bioorthogonal functionalization for bioanalytics with a spatial resolution in the one-micron range may be realized on solid supports compatible with fluorescence-based optical microscopy. The feature sizes of the silane nanodot arrays match well the length scales characteristic of a variety of biomolecular submicroscopic organizations in living cells, thus representing a compromise between miniaturization and the resolution limit of optical microscopy for sensitive high-throughput bioanalytics.

1 Introduction

Spatially controlled surface biofunctionalization at the micro- and nanoscale is a prerequisite for multiplexed bioanalytics, diagnostics and drug screening[1,2] as well as for systematic exploration of the role of spatial protein organization in cell biology.[3–5] Microcontact printing[6,7] and polymer pen lithography[8,9] combined with surface-initiated polymerization[10–13] are often employed for chemical surface patterning, enabling, for example, reversible modulation of biointerfacial interactions[14,15] and immobilization of biorecognition elements on protein-repellent polymer brushes.[16] Simple patterns such as

lines and squares are typically obtained by classical micro-contact printing,[17] whereas more complex patterns such as brush-polymer microarrays were obtained by polymer pen lithography.[18,19] The deformability of the elastomeric stamps used for chemical surface pattering limits the attainable resolutions and nearest-neighbor distances.[20,21] Reductions in the feature size require complex stamp configurations, such as composite stamps consisting of a harder contact surface connected to a softer support.[22] Most importantly, contact-lithographic methods relying on solid elastomeric stamps do not allow for *in situ* supply of ink to the contact surfaces of the stamps without interruption of the stamping operations.

Here we report the generation of ordered close-packed silane nanodot arrays with nanodot diameters of a few 100 nm and lattice constants in the one-micron range. To this end, we combined capillary nanostamping[23,24] onto glass slides with the binding of heterocyclic silanes introduced by Kim *et al.* to the glass surface *via* ring-opening triggered by surface hydroxyl groups[25,26] (Fig. 1). Nanobioanalytics by optical microscopy relies on monitoring of the fluorescence of analytes, probes, and labels. Direct attachment of heterocyclic silanes to hydroxyl-terminated substrate surfaces circumvents fluorescence quenching associated with classical thiol-on-gold chemistry. Moreover, on highly transparent glass substrates improved

[a]Institute for Chemistry of New Materials, Center for Cellular Nanoanalytics (CellNanOs), Universität Osnabrück, Barbarastr. 7, 49076 Osnabrück, Germany. E-mail: martin.steinhart@uos.de

[b]Department of Biology, Center for Cellular Nanoanalytics (CellNanOs), Universität Osnabrück, Barbarastr. 11, 49076 Osnabrück, Germany. E-mail: changjiang.you@biologie.uni-osnabrueck.de

[c]College of Life Sciences, Beijing University of Chemical Technology, 100029 Beijing, China

[d]Department of Physics, Universität Osnabrück, Barbarastr. 7, 49076 Osnabrück, Germany

† Electronic supplementary information (ESI) available: XPS measurements; supporting microscopic images. See DOI: 10.1039/c9ra03440d
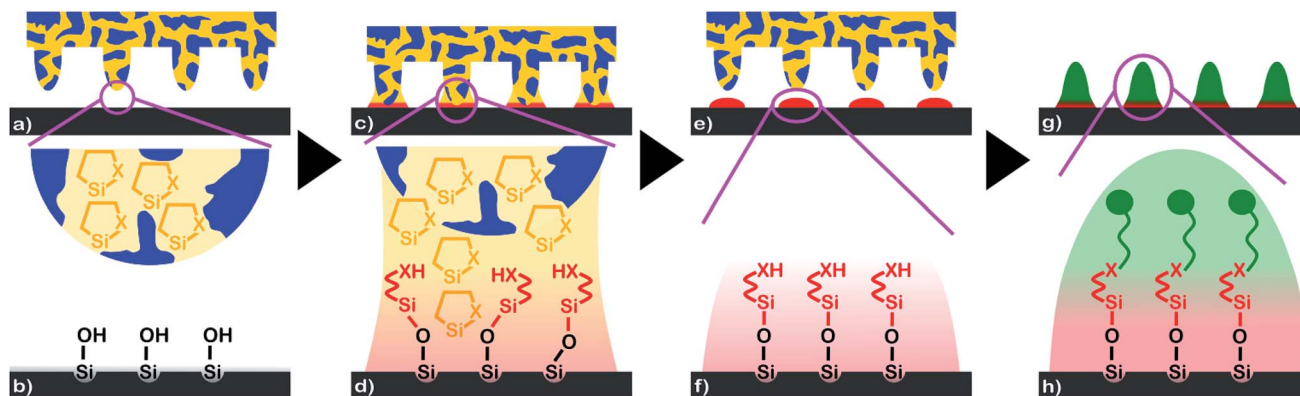
Fig. 1 Generation of silane nanodot arrays by capillary nanostamping of heterocyclic silanes coupled with substrate–initiated ring opening. (a) and (b) A spongy mesoporous silica stamp (blue) soaked with ink containing heterocyclic silanes (orange; X = heteroatom) approaches a glass slide (black) with hydroxyl–terminated surface. (c) and (d) Liquid ink bridges form at the positions of the stamp's contact elements. The hydroxyl groups at the glass surface trigger ring opening of the heterocyclic silanes. (e) and (f) At the positions of the contact elements nanodots consisting of a silane monolayer (red) bound to the glass surface form without byproducts. (g) and (h) The exposed terminal XH groups of the substrate-bound silane molecules enable further functionalization of the silane nanodots.

fluorescence signal-to-background contrast can be obtained. Hence, orthogonal biofunctionalization of the silane nanodots and the substrate areas surrounding them may yield substrates for sensitive high-throughput bioanalytics with micron-scale periodicity. Downscaling feature sizes on substrates for bio-analytics needs to be balanced with the need for reliable spatially resolved readout of processes of interest by optical microscopy. Arrays of silane nanodots with diameters of a few 100 nm and nearest-neighbor distances slightly above one micron represent a viable compromise between miniaturization and the resolution limit of optical microscopy. Furthermore, nearest-neighbor distances in the one-micron range match well the length scales characteristic of a variety of biomolecular submicroscopic organizations in living cells including membrane microcompartments, membrane-less organelles or protein phase separations[27] that play crucial roles for cell signaling and metabolism. Protein arrays obtained by specific immobilization of proteins-of-interest on the silane nanodots are ideal tools for deciphering the composition and spatio-temporal organization of microcompartmentalization at subcellular levels. In this way, protein aggregates,[28] liquid–liquid phase separation[29] and lipid phase separation within plasma membrane microcompartments[30] may be quantitatively assayed in living cells.

2 Experimental

2.1 Chemicals and materials

Dry toluene, dry dichloromethane (DCM), α-bromoisobutyryl bromide (BIBB), copper(II)bromide, N,N,N',N'',N''-penta-methyldiethylenetriamine (PMTDA) and tin(II) 2-ethylhexanoate were purchased from Alfa Aesar. Styrene, ethyl-α-bromoisobutyrate (EBIB), triethylamine (TEA) dimethylformamide (DMF) and ami-nopropyltrimethoxysilane (APTMS) were obtained from Sigma Aldrich. N-Aminoethyl-aza-2,2-dimethyl-4-methylsilacyclopentane (thereafter referred to as cycloazasilane) and 2,2-dimethoxy-1-

thia-2-silacyclopentane (thereafter referred to as cyclothiasilane) were purchased from Gelest. The fluorescent dyes ATTO 647 NHS and ATTO 655 maleimide were obtained from ATTO-TEC GmbH, Germany. Dibenzocyclooctyne-(polyethyleneglycol-12)-N-hydroxysuccinimidyl ester (NHS-PEG12-DBCO) was purchased from Click Chemistry Tools, USA. Azido-HaloTag-Ligand (click-HTL) was synthesized as described previously.[31] The IUPAC name of click-HTL is 3-(4-azidophenyl)-N-(2-(2-(6-chlorohexyloxy)ethoxy)ethyl)propanamide. HaloTag-fused monomeric enhanced GFP protein (HaloTag-mEGFP) and poly(L-lysine)-*graft*-poly-(ethylene glycol) terminated with methoxy groups (PLL-PEG-OMe) were prepared according protocols described previously.[32,33] Chemicals for preparing HEPES buffered saline (HBS), such as 4-(2-hydroxyethyl)-1-piperazineethanesulfonic acid and NaCl were purchased from Sigma Aldrich.

2.2 Capillary nanostamping

Spongy silica stamps with an area of 5 × 5 mm^2 and a thickness of 3 mm were prepared following procedures reported else-where.[23] The spongy silica stamps were immersed into toluene and then into the ink for ∼15 min. We used a 0.5 mM solution of the cycloazasilane, a 2 mM solution of the cyclothiasilane and a 2 mM APTMS solution in dry toluene as inks.

The glass slides to be stamped were treated with oxygen plasma for 10 min using a Diener femto plasma cleaner. The ink-infiltrated spongy silica stamps were attached to stamp holders with double-sided adhesive tape. As stamp holders we used stainless steel cylinders (height 4.5 cm; diameter 2 cm; mass ∼ 27 g) with a flat cylinder base and an additional 3 mm thick poly(dimethylsiloxane) (PDMS) layer between stamp and base. After capillary nanostamping, the patterned glass slides were rinsed with toluene and ethanol to remove unreacted silane molecules. Silane nanodots obtained by capillary nano-stamping of cycloazasilane are thereafter referred to as amino-silane nanodots and silane nanodots obtained by capillary nanostamping of cyclothiasilane as thiosilane nanodots.

2.3 Post-stamping treatments

2.3.1 Fluorescent labelling. Aminosilane nanodots were labeled with a 0.5 μM solution of ATTO 647 NHS in HBS (20 mM HEPES; pH 7.5; 150 mM NaCl) for 10 min. The samples were then washed with MilliQ water for three times. The same procedure was applied to label thiosilane nanodots, the difference being that ATTO 655 maleimide was used as fluorescent dye. APTMS nanodots were labelled with a solution of 1 μM ATTO 647 NHS in HBS buffer for 10 min.

2.3.2 Synthesis of PS brushes. Glass slides patterned with arrays of aminosilane nanodots were immersed into a mixture of 5 mL dry DCM, 123 μL BIBB (1 mmol) and 207 μL TEA (1.5 mmol) for 12 h under shaking. Then, the glass slides were washed with DCM, H_2O and EtOH. 5 mL styrene was subjected to column chromatography using basic alumina as stationary phase to remove stabilizers, collected in a flask and degassed with argon for 30 min. The prepared glass slides, 3.2 μL EBIB (0.02 mmol), 181 μL of a $CuBr_2$/DMF solution (0.1 M) and 181 μL of a PMDTA/DMF solution (0.5 M) were added under argon. The flask was sealed with a septum cap and heated to 90 °C. 271 μL Sn(II) 2-ethylhexanoate (0.8 mmol) was added through the septum cap to start the reaction. After a polymerization time of 7 h the reaction mixture became viscous and the reaction was stopped by cooling to room temperature and exposure of the catalyst to air. The glass slides were ultrasonicated in methanol, ethanol, DCM and DMF for 15 min to remove excess polymer.

2.3.3 Immobilization of HaloTag-fused mEGFP protein. Aminosilane nanodots stamped on glass slides were functionalized with 1 μM DBCO-PEG12-NHS in HBS for 15 min. After the coupling reaction, the glass slides were washed with H_2O, MeOH and EtOH. The DBCO moiety was clicked with a 1 μM solution of Azido-HaloTag Ligand (click-HTL)[31] in DMF for 2 h and washed with DMF and EtOH. After drying in a nitrogen stream, the unprotected surface of the glass slides between the aminosilane nanodots was backfilled with a PLL-PEG-OMe solution in HBS buffer (2 mg mL^{-1}) for 10 min and washed with fresh MilliQ water. For protein immobilization, the slides were incubated with HBS buffer containing 200 nM HaloTag-mEGFP for 5 min and washed repeatedly with HBS. The obtained samples were stored in HBS before TIRFM imaging.

2.4 Characterization

2.4.1 X-ray photoelectron spectroscopy (XPS). XPS measurements were carried out under ultra-high vacuum in an ESCA-unit Phi 5000 VersaProbe III with a base pressure of 10^{-9} mbar. As X-ray source the Al K$_\alpha$ radiation of a monochromatized Al anode ($h\nu = 1486.6$ eV) was used. Sample charging was prevented by using simultaneously both an ion gun and an electron gun. The signals were analysed with a 32-channel electrostatic hemispherical electronic analyser. The take-off angle enclosed by the sample surface and a line connecting detection volume and analyser was varied (15°–65°) to discriminate contributions of the silica substrates and the aminosilane nanodot arrays. Here, we present spectra acquired at a take-off angle of 15° to enhance the contribution of the aminosilane nanodot arrays. The XP spectra were calibrated using the carbon C 1s (185.0 eV) peak.[34] For analysing and fitting the XP spectra we used the software XPSPeak 4.1.

2.4.2 Water contact angle measurements. For water contact angle measurements, we used a drop shape analyzer Krüss DSA100 operated in the sessile drop mode at 23 °C and a humidity of 46%.

2.4.3 Scanning electron microscopy (SEM). Scanning electron microscopy images were acquired with a Zeiss Auriga scanning electron microscope operated at an accelerating voltage of 3 keV. Before imaging, the samples were sputter-coated with platinum/iridium.

2.4.4 Atomic force microscopy (AFM). Atomic force microscopy was performed in the semicontact mode using a NT-MDT NTEGRA microscope with NSG10 cantilevers purchased from NT-MDT (silicon; tip curvature < 10 nm; resonant frequency between 140 kHz and 390 kHz; force constant between 3.1 N m^{-1} and 37.6 N m^{-1}).

2.4.5 Total internal reflection fluorescence microscopy (TIRFM). TIRFM was carried out at ambient temperature using an inverted microscope (Olympus IX71) equipped with a 4-Line TIRF condenser (Olympus TIRF 4-Line). A 488 nm diode laser (LuxX 488-200, Omicron) was used for the imaging of samples functionalized with HaloTag-mEGFP. A 642 nm diode Laser (LuxX 642-100, Omicron) was used for the imaging of samples functionalized with ATTO 647 NHS and ATTO 655 maleimide. The lasers were operated in combination with a TIRF pentaband polychroic beamsplitter (Semrock zt405/488/561/640/730rpc) and a pentabandpass emitter (Bright-Line HC 440/521/607/694/809). Images were acquired with an electron multiplying CCD camera (Andor iXon Ultra 897) through a 150-fold oil immersion objective (Olympus UAPON 150x TIRF, NA 1.45).

2.4.6 Analysis and processing of TIRFM images. The TIRFM images were deconvolved with a theoretical point spread function (PSF) for wide field microscopes using the software Huygens (Huygens Core, Software Version 18.4.1, Scientific Volume Imaging, Netherlands, http://svi.nl). The following settings were applied: deconvolution algorithm = classic maximum likelihood estimation (CMLE); background mode = automatic; signal to noise ratio (SNR) = 30; number of iterations = 20; quality change number = 0.01. Local intensity maxima in the Gaussian-smoothed deconvolved TIRFM images were recognized as potential silane nanodots. For each potential silane nanodot at first the distances to its 6 nearest neighbours and subsequently the median values of the obtained 6 nearest-neighbour distances were calculated. Potential silane nanodots were accepted for final analysis if all 6 nearest-neighbour distances had values 0.8–1.2 times as large as the median nearest-neighbour distance. The medians of all median nearest-neighbour distances belonging to accepted silane nanodots were considered as lattice constants of the silane nanodot arrays. The nanodot diameters were fitted with an isotropic 2D-Gaussian[35] using Matlab Version 2016b.

3   Results and discussion

3.1   Capillary nanostamping of heterocyclic silanes: principle

Classical agents for surface modification – such as trifunctional alkoxysilanes, carboxysilanes and chlorosilanes – undergo hydrolytic condensation and are prone to polymerization triggered by water. Polymerization may occur close to and away from a substrate surface to be modified.[36] Monofunctional and bifunctional noncyclic silanes, on the other hand, frequently lack the required reactivity. We used inks containing heterocyclic silanes that have recently emerged as a new class of agents for highly precise modification of hydroxyl-terminated surfaces. Cyclic azasilanes containing Si–N bonds and cyclic thiosilanes containing Si–S bonds in their rings undergo click-chemical ring-opening reactions triggered by –OH groups on silica surfaces.[25,26] The ring-opening is coupled with hydrogen transfer from the surface hydroxyl groups to the heteroatom X of the heterocyclic silanes. As a result, precisely one heterocyclic silane molecule per surface hydroxyl group will bind to the substrate surface. Polymerization of the heterocyclic silanes is intrinsically not possible. We moreover assume that heterocyclic silane molecules react with residual water the ink may contain. The heterocyclic silanes themselves thus remove water from the ink, while the resulting hydrolysis products do not bind to the silica surface or impede the surface-initiated ring-opening of the remaining heterocyclic silane molecules. Hence, silane monolayers having exposed terminal –XH groups form without byproducts.

Capillary nanostamping was carried out with spongy mesoporous silica stamps prepared *via* the sol–gel route following procedures reported elsewhere[23,37] using methyltrimethoxysilane[37] as silica precursor. The spongy mesoporous silica stamps had methyl-terminated pore walls resistant against organic solvents and inert towards the heterocyclic silanes. Their contact surfaces were topographically patterned with regular hexagonal arrays of conical contact elements (base diameter $\sim$ 600 nm; tip diameter $\sim$ 400 nm; height $\sim$ 500 nm; nearest neighbour distance 1.2–1.3 μm; average pore diameter $\sim$ 31 nm) (*cf.* ESI Fig. S1† and ref. 23).

We infiltrated the spongy mesoporous silica stamps with solutions of the heterocyclic silanes in toluene and glued them onto cylindrical stamp holders. Capillary nanostamping with a contact time of less than 1 s was performed manually and under ambient conditions by bringing the topographically patterned contact surfaces of the spongy mesoporous silica stamps in contact with the surfaces of glass slides (Fig. 1a and b; for a photograph see ESI Fig. S2†). Ring opening by a reaction with the surface hydroxyl groups converted the heterocyclic silanes into XH-terminated non-cyclic alkyl silanes bound to the surfaces of the glass slides at the positions of the stamps' contact elements (Fig. 1c and d). As a result, nanodots with diameters of a few 100 nm consisting of silane monolayers form at the positions of the stamps' contact elements (Fig. 1e and f). Since the spongy mesopore system acts as ink reservoir and allows *in situ* ink supply, multiple successive stamping cycles can be performed under ambient conditions without

interruptions for re-inking and without deterioration of the pattern quality. It should be noted that, in contrast to typical procedures used for polymer pen lithography, each single contact between a mesoporous silica stamp and a substrate already yields a complete silane nanodot array with a nearest-neighbour distance in the 1 μm range. A series of capillary nanostamping cycles carried out at different positions on a substrate or on different substrates yields, therefore, the corresponding number of separate silane nanodot arrays. The exposed terminal –XH groups of the silane molecules forming the nanodots enable further functionalization (Fig. 1g and h).

3.2   Capillary nanostamping of heterocyclic silanes: results

Stamping the cycloazasilane *N*-aminoethyl-aza-2,2-dimethyl-4-methylsilacyclopentane (X = N–CH$_2$–CH$_2$–NH$_2$) in toluene onto glass slides resulted in the formation of [*N*-(2-aminoethyl)-2-methyl-3-aminopropyl]dimethylsilane nanodots (aminosilane nanodots) at the contact sites of the spongy mesoporous silica stamps by the ring-opening reaction sketched in Fig. 2a. A phenomenological signature of the presence of aminosilane nanodot arrays is an increase in the water contact angle, which amounts to 0° on unmodified glass slides. We measured the water contact angle on three aminosilane nanodot arrays that were successively stamped without reinking the mesoporous silica stamp and obtained water contact angles of 70.7°, 72.1° and 73.3°.

XPS is frequently used to characterize silane layers on solid substrates. Thus, we measured XP spectra of areas in which the glass slides were patterned with aminosilane nanodot arrays and, for comparison, of nonpatterned areas in between. We acquired the XP spectra varying the take-off angle to distinguish contributions from the silica substrates and from the aminosilane nanodot arrays. Here, we present XP spectra obtained with a low electron take-off angle of 15° in order to enhance the surface sensitivity of the XPS measurements. The Si 2p peak of Si atoms incorporated into silica networks, which is attributed to Si in the oxidation state 4+, appears at a binding energy (BE) of $\sim$103.5 eV.[38,39] In XP spectra of nonpatterned areas covering the corresponding BE region (ESI Fig. S3a†), a Si 2p peak with a maximum at 103.3 eV is detected that can be ascribed to silica-Si. The Si 2p peak originating from silane-Si has a maximum shifted to slightly lower BE values of 102.3–102.5 eV, since silane-Si is in the lower oxidation state 3+.[38,39] If silanes on a silica surface are probed, the position of the Si 2p peak maximum lies between the positions of the peak maxima originating from silica-Si and from silane-Si.[40] The XP spectrum seen in ESI Fig. S3b† was measured on an aminosilane nanodot array, which was located on the same glass slide as the nonpatterned area of which the XP spectrum seen in ESI Fig. S3a† was taken. The slight shift of the Si 2p peak maximum to a lower BE value of 102.9 eV in the XP spectrum of the aminosilane nanodot array indicates the presence of silane-Si. We decomposed the Si 2p peak obtained on the aminosilane nanodot array into two Lorentzian functions representing the contributions of silica-Si and silane-Si. The peak maximum of the silica-Si contribution was set to 103.3 eV, corresponding to the
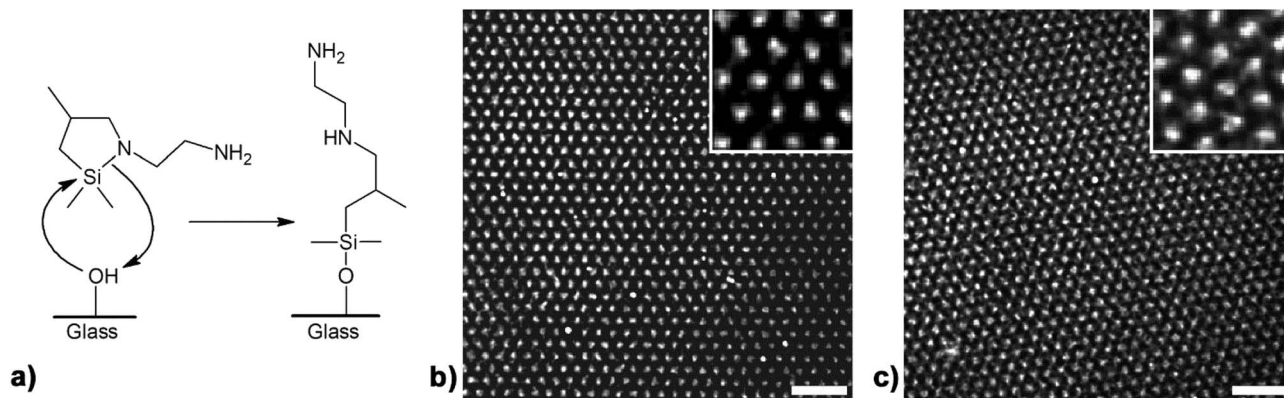
Fig. 2 Capillary nanostamping of *N*-aminoethyl-aza-2,2-dimethyl-4-methylsilacyclopentane in toluene onto glass slides. (a) Reaction scheme of the ring opening reaction with the surface hydroxyl groups. (b) and (c) TIRFM images of aminosilane nanodot arrays stamped onto glass slides after binding the dye ATTO 647 NHS to the terminal amine groups of the silanes. (b) 4th and (c) 10th consecutive stamping cycle under ambient conditions without reinking. The raw TIRFM images were deconvolved using the Huygens software. The scale bars correspond to 5 μm. Insets are zoom-in regions of 5 × 5 μm².

maximum of the Si 2p peak obtained for nonpatterned glass. The relative peak area of the silica-Si contribution amounted to 60%. The silane-Si contribution had a peak maximum at 102.5 eV and a relative peak area of 40%. However, the Lorentzian fits should be considered rather as a rough approach to the atomic number ratio silica-Si/silane-Si than as a precise determination of the latter due to the unknown escape depth of the photoelectrons from the silica substrates and the aminosilane nanodot arrays. We also recorded XP spectra in the BE region where the nitrogen 1s peak is located. While no indication for the presence of nitrogen was apparent in the XP spectrum recorded on nonpatterned glass, a N 1s peak at ∼400.5 eV originating from the aminosilane nitrogen atoms is clearly present in the XP spectrum of the aminosilane nanodot array (ESI Fig. S4†). Finally, the C 1s peak obtained from the aminosilane nanodot array shows, in contrast to the C 1s peak

originating from adventitious carbon in the non-patterned area (with a binding energy of 185.0 eV), a shoulder at the higher-BE side (ESI Fig. S5a†). We fitted the sum of two Lorentzian contributions to the C 1s peak obtained from the aminosilane nanodot array (ESI Fig. S5b†). We assumed that the maximum of the C 1s peak originating from aminosilane methyl and methylene carbon atoms away from the more electronegative binding partner nitrogen equals the C 1s peak maximum obtained for adventitious carbon in the nonpatterned area. The second contribution shifted to higher BE values (peak maximum at 286.7 eV) can be ascribed to methylene carbon atoms in α-position to one of the amino groups.[41] An aminosilane molecule contains 3 carbon atoms directly bound to nitrogen (38%) and 5 carbon atoms not bound to nitrogen (62%). The relative peak area of the Lorentzian function at higher BE values amounts to 28% and that of the Lorentzian
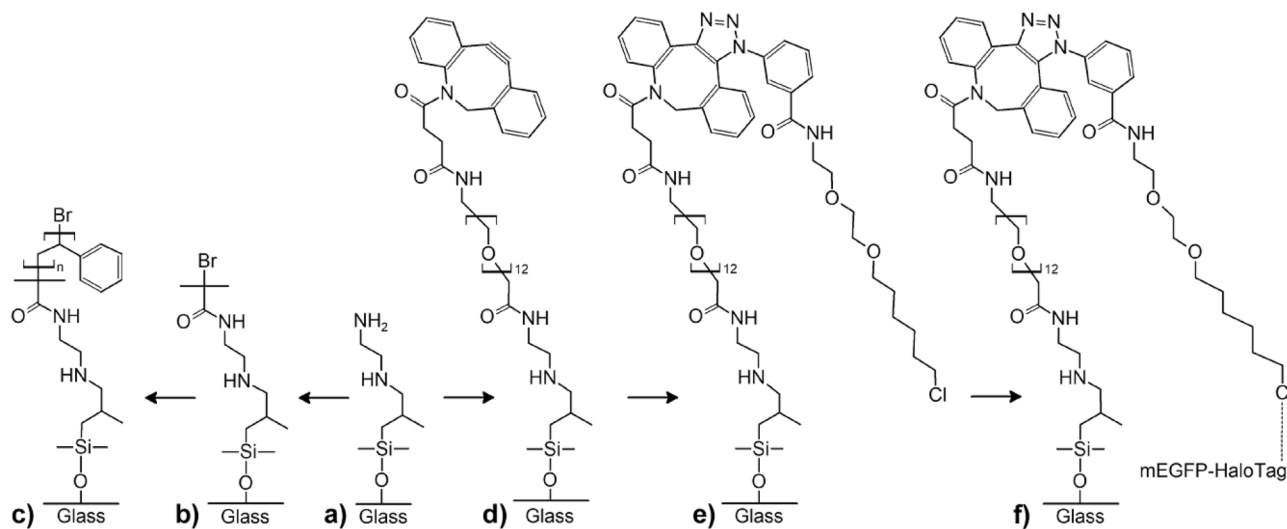

Fig. 3 Functionalization of aminosilane nanodots. (a)–(c) Reaction scheme for the synthesis of PS nanobrushes at the positions of the aminosilane nanodots. (d)–(f) Reaction scheme for the functionalization of the aminosilane nanodots with HaloTag-fused monomeric enhanced green fluorescence protein.

function at lower BE values to 72%. Considering that adventitious carbon may contribute to the Lorentzian function at lower BE values, this peak area ratio is in reasonable agreement to the atomic number ratio. Overall, the results of the contact angle and XPS measurements corroborate the notion that the cyclo-azasilane molecules bind to the glass substrates during capillary nanostamping.

3.3 Dye-labelled aminosilane nanodot arrays: TIRFM

Arrays of aminosilane nanodots were further functionalized by attaching the dye ATTO 647 NHS to the terminal amine groups of the aminosilanes (Fig. 2a) and then imaged by TIRFM. The feature sizes of the silane nanodot arrays were not properly resolved in the raw images (ESI Fig. S6†) due to diffraction limitation. Therefore, we deconvolved the raw TIRFM images using the Huygens image processing software that takes the point spread function of the microscope into account. Deconvolved images of ATTO 647 NHS-functionalized aminosilane nanodot arrays obtained in the 4th and the 10th successive

stamping cycles without reloading the spongy mesoporous silica stamp with ink are shown in Fig. 2b and c, respectively. The diameters of the aminosilane nanodots were determined from the deconvolved images by fitting isotropic 2D-Gaussians.[35] For the 4th consecutive stamping cycle (Fig. 2b) we obtained a median nanodot diameter of 356 nm $\pm$ 51 nm and a nearest neighbour median distance of 1.31 μm $\pm$ 0.02 μm. For the 10th consecutive stamping cycle (Fig. 2c), we obtained a median nanodot diameter of 376 nm $\pm$ 60 nm and a nearest neighbour median distance of 1.30 μm $\pm$ 0.02 μm. Capillary nanostamping of 2,2-dimethoxy-1-thia-2-silacyclopentane onto glass slides correspondingly yielded arrays of dimethoxy-(3-thiopropyl)silane nanodots (ESI Fig. S7†). TIRFM imaging after binding the dye ATTO 655 maleimide to the terminal thiol groups yielded median nanodot diameters of 314 nm $\pm$ 58 nm (1st stamping cycle), 318 nm $\pm$ 52 nm (4th stamping cycle), 334 nm $\pm$ 64 nm (7th stamping cycle) and 342 nm $\pm$ 60 nm (10th stamping cycle).
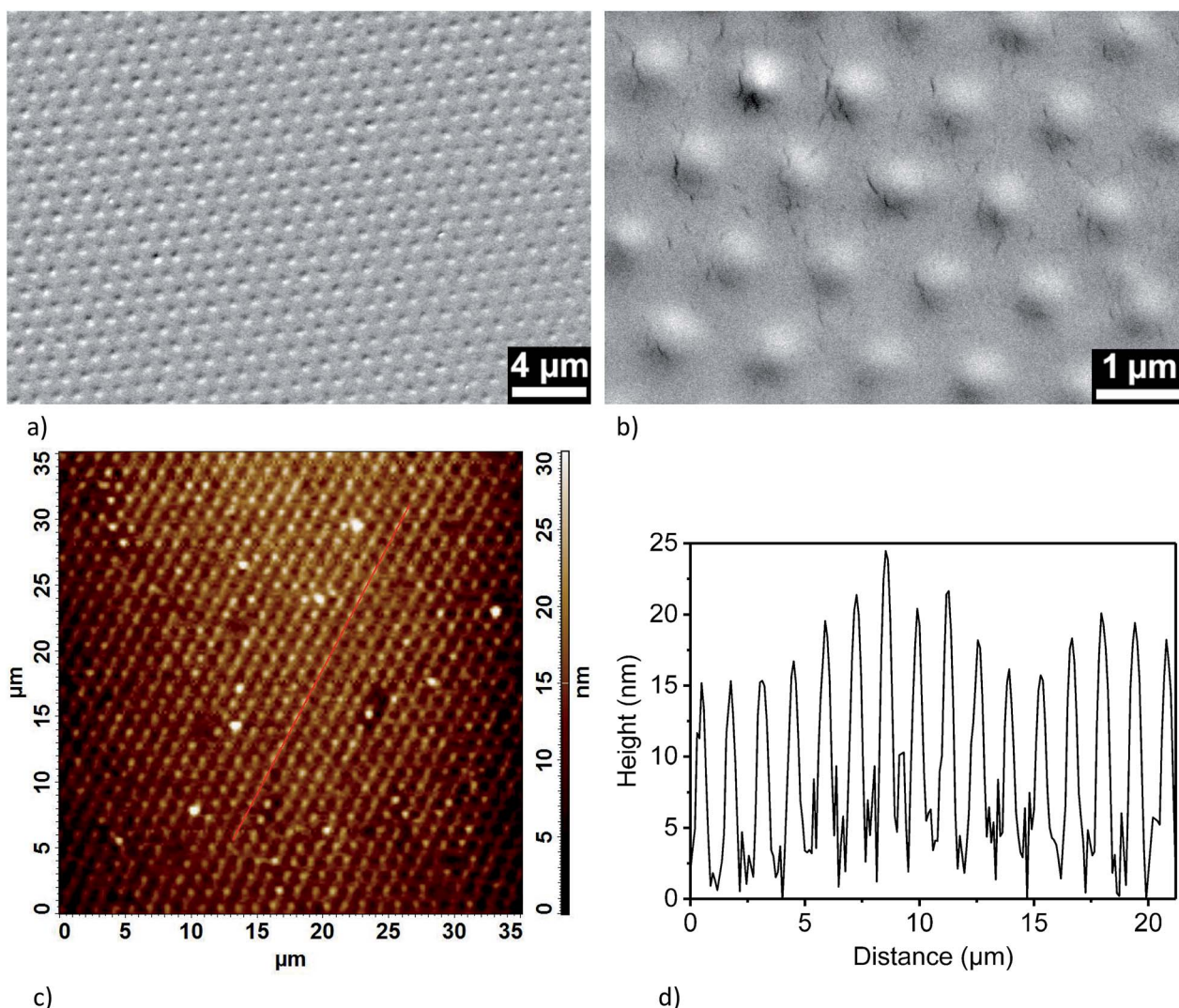

Fig. 4 Functionalization of aminosilane nanodot arrays with PS nanobrushes *via* ARGET ATRP. (a) and (b) SEM images of an array of PS nanobrushes. (a) Overview; (b) detail. (c) AFM image of the topography of a PS nanobrush array. (d) Topographic profile along the line in panel (c).

We could typically perform more than 10 successive stamping cycles under ambient conditions without reloading the spongy mesoporous silica stamps with ink and without deterioration of the quality of the generated silane nanodot arrays. Capillary nanostamping of heterocyclic silanes, even when carried out manually under ambient conditions, is robust with respect to variations in contact time and contact pressure. Within a series of 10 successive stamping cycles the nanodot median diameter typically scatters by ±5%. A reason for this robustness – as compared to manual stamping with elastomeric stamps – might be the rigidity of the contact elements of the mesoporous silica stamps. While the contact elements of elastomeric stamps consisting of materials such as cross-linked PDMS may deform upon contact formation with the substrate, the contact elements of the mesoporous silica stamps retain their shape. It should be noted that under the well-controlled conditions of polymer pen lithography (controlled atmosphere, parallel adjustment of stamp and substrate, controlled load during stamping) more precise control over pattern sizes is achievable.[42] We assume that the nanodot size depends first and foremost on the geometry of the stamp's contact elements, which crucially affects the interplay of contact line movement of the liquid ink bridges at the contact elements, solvent evaporation and adsorption of the non-volatile ink components on the substrate. If, for example, mesoporous stamps with regular arrays of wells are used, correspondingly ordered holey films of the non-volatile ink components are obtained.[43]

Capillary nanostamping of "classical" trifunctional silane coupling agents – while, in principle, possible – may suffer from oligo- and polymerization of the silanes. For example, we stamped the trifunctional alkoxysilane APTMS under ambient conditions onto glass slides and bound ATTO 647 NHS to the terminal APTMS amino groups. The first stamping cycle yielded a regular array of APTMS nanodots with a median diameter of 298 nm ± 20 nm and a nearest neighbour median distance of 1.397 μm ± 10 nm (ESI Fig. S8a†). However, in the following stamping cycles carried out immediately thereafter the quality of the obtained patterns markedly deteriorated. In the TIRFM image of the pattern resulting from the fourth successive stamping cycle shown in ESI Fig. S8b,† only 9 features met the quality criteria for APTMS nanodots (cf. Section 2.4.6). Hence, we could not determine the median values of the nanodot diameter and nearest neighbour distance.

3.4 Chemical functionalization of aminosilane nanodots

The terminal functional groups of the silane molecules forming the nanodots also enable more complex chemical functionalizations (Fig. 3). For a proof-of-concept, we synthesized polystyrene (PS) brushes at the positions of the aminosilane nanodots by adapting protocols reported by Li et al.[44] based on surface-initiated atom-transfer radical polymerization (ATRP) combined with a process referred to as "activators regenerated by electron transfer" (ARGET)[45] (Fig. 3a–c). We coupled α-bromoisobutyryl bromide (BIBB) to the terminal amine groups of the aminosilane nanodots (Fig. 3b) to generate initiation sites for the synthesis of PS (Fig. 3c). Thus, we obtained regular large-area arrays of discrete PS nanobrushes (Fig. 4a and b, for larger-area SEM images see ESI Fig. S9†). The PS nanobrushes had diameters of ~600 nm and heights of ~15 nm, as determined from AFM topography images (Fig. 4c and d). No backfilling was necessary to obtain the arrays of PS nanobrushes.

We could also demonstrate bio-orthogonal functionalization with an about tenfold improved spatial resolution as compared to conventional soft lithography for biofunctionalization[32,46,47] by site-specific protein immobilization at the aminosilane nanodots via the HaloTag (Fig. 3a and d–f). Aminosilane nanodots were first reacted with dibenzocyclooctyne (DBCO)-NHS (Fig. 3d) and subsequently functionalized with azido-HaloTag-Ligand (click-HTL)[31] by copper-free click chemistry (Fig. 3e). After backfilling with PLL-PEG-OMe to inhibit nonspecific protein binding around the aminosilane nanodots, monomeric enhanced green fluorescent protein fused to the HaloTag (HaloTag-mEGFP)[32,33] was immobilized on the click-HTL-functionalized aminosilane nanodots (Fig. 3f). Surface binding of HaloTag-mEGFP to click-HTL was calculated using a pseudo-first order model according to $\Gamma = 1 - e^{-k_{on}Ct}$, where Γ is the surface load of HaloTag-mEGFP, C the concentration of HaloTag-mEGFP in solution and t the incubation time. We set the on-rate constant of HaloTag-mEGFP binding to click HTL k_{on} to the previously determined value of $4 \times 10^4 \, \mathrm{M^{-1} \, s^{-1}}$.[31] The HaloTag-mEGFP concentration and the incubation time applied here ensured 91% click-HTL binding with HaloTag-mEGFP protein, as confirmed by TIRFM imaging (ESI Fig. S10†). The deconvolved TIRFM image shown in Fig. 5 contains an array bright aminosilane nanodots functionalized with HaloTag-mEGFP marked by mEGFP fluorescence. The aminosilane nanodots functionalized with HaloTag-mEGFP
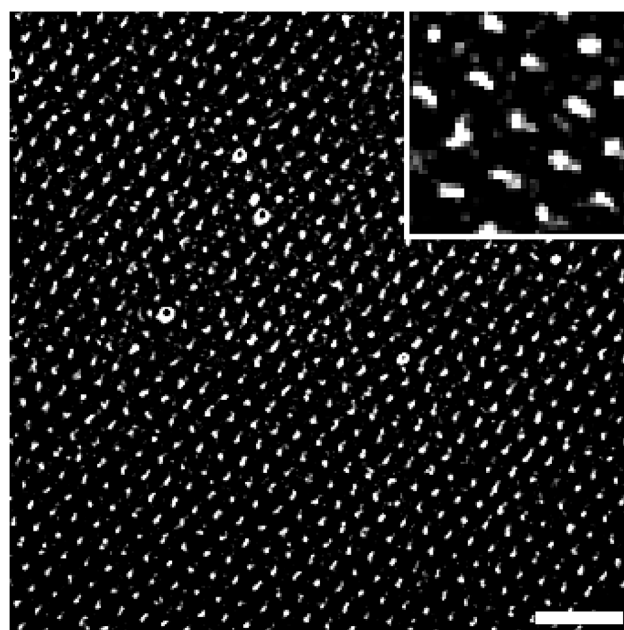

Fig. 5 TIRFM image of an aminosilane nanodot array functionalized with Halo-Tag®/mEGFP showing mEGFP fluorescence. The raw TIRFM image was deconvolved using the Huygens software (scale bar = 5 μm; the inset is a zoom-in region of 5 × 5 μm²).

had an apparent median diameter of 220 nm $\pm$ 38 nm and a nearest-neighbour spacing of 1.32 μm.

4 Conclusions

In conclusion, the combination of manual capillary nano-stamping under ambient conditions using spongy mesoporous silica stamps and lithographic surface modification *via* surface-initiated ring opening of heterocyclic silanes yielded close-packed arrays of discrete functionalizable silane nanodots with diameters of a few 100 nm and nearest-neighbour distances of 1.2–1.3 μm. These geometric array parameters match well the length scales characteristic of a variety of biomolecular submicroscopic organizations in living cells and represent a compromise between miniaturization and the resolution limit of optical microscopy. Since the stamps' spongy mesopore systems act as ink reservoir and can be used for *in situ* ink supply, multiple successive stamping cycles can be carried out without interruptions caused by ink depletion. The heterocyclic silanes bind to the surfaces of glass slides at the positions of the stamps' contact elements *via* ring opening triggered by the surface hydroxyl groups. Thus, the silane nanodots consisted of monolayers of silane molecules with exposed functional groups for further functionalization. Exemplary functionalizations of the silane nanodots included the generation of arrays of polymer nanobrushes by surface-initiated ATRP and the immobilization of proteins *via* conjugation of dibenzocyclooctyne to the silane nanodots to enable copper-free click reactions with azide derivatives. Avoiding gold substrates that impede fluorescence emission, the configuration reported here potentially enables orthogonal bio-functionalization for fluorescence-based nanobioanalytics combined with spatial resolutions in the one-micron range. The obtained 10-fold-improved spatial resolution in comparison to conventional micropatterned bioanalytic arrays results in an increase in the areal density of discrete cell–substrate interaction sites by two orders of magnitude.

Conflicts of interest

There are no conflicts to declare.

Acknowledgements

Notes and references

1 D. Weinrich, P. Jonkheijm, C. M. Niemeyer and H. Waldmann, *Angew. Chem., Int. Ed.*, 2009, **48**, 7744–7751.

2 S. Schumacher, S. Muekusch and H. Seitz, *Microarrays*, 2015, **4**, 196–213.

3 H. Cai, J. Muller, D. Depoil, V. Mayya, M. P. Sheetz, M. L. Dustin and S. J. Wind, *Nat. Nanotechnol.*, 2018, **13**, 610–617.

4 T. Satav, J. Huskens and P. Jonkheijm, *Small*, 2015, **11**, 5184–5199.

5 V. Hortiguela, E. Larranaga, F. Cutrale, A. Seriola, M. Garcia-Diaz, A. Lagunas, J. Andilla, P. Loza-Alvarez, J. Samitier, S. Ojosnegros and E. Martinez, *Nano Lett.*, 2018, **18**, 629–637.

6 G. M. Whitesides, E. Ostuni, S. Takayama, X. Y. Jiang and D. E. Ingber, *Annu. Rev. Biomed. Eng.*, 2001, **3**, 335–373.

7 Y. Xia and G. M. Whitesides, *Annu. Rev. Mater. Sci.*, 1998, **28**, 153–184.

8 F. Huo, Z. Zheng, G. Zheng, L. R. Giam, H. Zhang and C. A. Mirkin, *Science*, 2008, **321**, 1658–1660.

9 C. Carbonell and A. B. Braunschweig, *Acc. Chem. Res.*, 2017, **50**, 190–198.

10 I. W. Moran, J. R. Ell and K. R. Carter, *Small*, 2011, **7**, 2669–2674.

11 B. Li, B. Yu, Q. Ye and F. Zhou, *Acc. Chem. Res.*, 2015, **48**, 229–237.

12 Q. Yu, L. K. Ista, R. P. Gu, S. Zauscher and G. P. Lopez, *Nanoscale*, 2016, **8**, 680–700.

13 W. L. Chen, R. Cordero, H. Tran and C. K. Ober, *Macromolecules*, 2017, **50**, 4089–4113.

14 Q. Yu, P. Shivapooja, L. M. Johnson, G. Tizazu, G. J. Leggett and G. P. Lopez, *Nanoscale*, 2013, **5**, 3632–3637.

15 Q. Yu, J. Cho, P. Shivapooja, L. K. Ista and G. P. Lopez, *ACS Appl. Mater. Interfaces*, 2013, **5**, 9295–9304.

16 U. Bog, A. D. Pereira, S. L. Mueller, S. Havenridge, V. Parrillo, M. Bruns, A. E. Holmes, C. Rodriguez-Emmenegger, H. Fuchs and M. Hirtz, *ACS Appl. Mater. Interfaces*, 2017, **9**, 12109–12117.

17 T. Pompe, A. Fery, S. Herminghaus, A. Kriele, H. Lorenz and J. P. Kotthaus, *Langmuir*, 1999, **15**, 2398–2401.

18 S. D. Bian, S. B. Zieba, W. Morris, X. Han, D. C. Richter, K. A. Brown, C. A. Mirkin and A. B. Braunschweig, *Chem. Sci.*, 2014, **5**, 2023–2030.

19 Z. Xie, C. J. Chen, X. C. Zhou, T. T. Gao, D. Q. Liu, Q. Miao and Z. J. Zheng, *ACS Appl. Mater. Interfaces*, 2014, **6**, 11955–11964.

20 A. Perl, D. N. Reinhoudt and J. Huskens, *Adv. Mater.*, 2009, **21**, 2257–2268.

21 J. L. Hedrick, K. A. Brown, E. J. Kluender, M. D. Cabezas, P. C. Chen and C. A. Mirkin, *ACS Nano*, 2016, **10**, 3144–3148.

22 M. A. Verschuuren, M. Megens, Y. Ni, H. van Sprang and A. Polman, *Adv. Opt. Technol.*, 2017, **6**, 243–264.

23 M. Schmidt, M. Philippi, M. Münzner, J. M. Stangl, R. Wieczorek, W. Harneit, K. Müller-Buschbaum, D. Enke and M. Steinhart, *Adv. Funct. Mater.*, 2018, **28**, 1800700.

24 W. Han, P. Hou, S. Sadaf, H. Schäfer, L. Walder and M. Steinhart, *ACS Appl. Mater. Interfaces*, 2018, **10**, 7451–7458.

25 D. Kim, J. M. Zuidema, J. Kang, Y. Pan, L. Wu, D. Warther, B. Arkles and M. J. Sailor, *J. Am. Chem. Soc.*, 2016, **138**, 15106–15109.

26 Y. L. Pan, A. Maddox, T. Min, F. Gonzaga, J. Goff and B. Arkles, *Chem.–Asian J.*, 2017, **12**, 1198–1203.

27 S. Boeynaems, S. Alberti, N. L. Fawzi, T. Mittag, M. Polymenidou, F. Rousseau, J. Schymkowitz, J. Shorter, B. Wolozin, L. Van Den Bosch, P. Tompa and M. Fuxreiter, *Trends Cell Biol.*, 2018, **28**, 420–435.

28 G. Simic, M. Babic Leko, S. Wray, C. Harrington, I. Delalle, N. Jovanov-Milosevic, D. Bazadona, L. Buee, R. de Silva, G. Di Giovanni, C. Wischik and P. R. Hof, *Biomolecules*, 2016, **6**, 6.

29 S. Ambadipudi, J. Biernat, D. Riedel, E. Mandelkow and M. Zweckstetter, *Nat. Commun.*, 2017, **8**, 275.

30 A. Honigmann and A. Pralle, *J. Mol. Biol.*, 2016, **428**, 4739–4748.

31 D. Liße, V. Wilkens, C. You, K. Busch and J. Piehler, *Angew. Chem., Int. Ed.*, 2011, **50**, 9352–9355.

32 T. Wedeking, S. Löchte, C. P. Richter, M. Bhagawati, J. Piehler and C. You, *Nano Lett.*, 2015, **15**, 3610–3615.

33 T. Wedeking, S. Löchte, O. Birkholz, A. Wallenstein, J. Trahe, J. Klingauf, J. Piehler and C. You, *Small*, 2015, **11**, 5912–5918.

34 T. L. Barr and S. Seal, *J. Vac. Sci. Technol., A*, 1995, **13**, 1239–1246.

35 A. Serge, N. Bertaux, H. Rigneault and D. Marguet, *Nat. Methods*, 2008, **5**, 687–694.

36 S. Onclin, B. J. Ravoo and D. N. Reinhoudt, *Angew. Chem., Int. Ed.*, 2005, **44**, 6282–6304.

37 K. Kanamori, M. Aizawa, K. Nakanishi and T. Hanada, *Adv. Mater.*, 2007, **19**, 1589–1593.

38 K. M. R. Kallury, J. D. Brennan and U. J. Krull, *Anal. Chem.*, 1995, **67**, 2625–2634.

39 Y. C. Araujo, P. G. Toledo, V. Leon and H. Y. Gonzalez, *J. Colloid Interface Sci.*, 1995, **176**, 485–490.

40 T. J. Horr and P. S. Arora, *Colloids Surf., A*, 1997, **126**, 113–121.

41 X. P. Cao and R. J. Hamers, *J. Vac. Sci. Technol., B: Microelectron. Nanometer Struct.–Process., Meas., Phenom.*, 2002, **20**, 1614–1619.

42 X. Liao, A. B. Braunschweig, Z. Zheng and C. A. Mirkin, *Small*, 2010, **6**, 1082–1086.

43 L. Guo, M. Philippi and M. Steinhart, *Small*, 2018, **14**, 1801452.

44 Y. M. Li, Q. Li, C. Q. Zhang, P. Cai, N. N. Bai and X. Xu, *Chem. Eng. J.*, 2017, **323**, 134–142.

45 K. Matyjaszewski, H. C. Dong, W. Jakubowski, J. Pietrasik and A. Kusumo, *Langmuir*, 2007, **23**, 4528–4531.

46 K.-i. Arimoto, S. Löchte, S. A. Stoner, C. Burkart, Y. Zhang, S. Miyauchi, S. Wilmes, J.-B. Fan, J. J. Heinisch, Z. Li, M. Yan, S. Pellegrini, F. Colland, J. Piehler and D.-E. Zhang, *Nat. Struct. Mol. Biol.*, 2017, **24**, 279–289.

47 C. Dirscherl, R. Palankar, M. Delcea, T. A. Kolesnikova and S. Springer, *Small*, 2017, **13**, 1602974.